

# Carrier Mobilities in $\delta$ -doped Heterostructures

Y. Shao and S. A. Solin\*  
*Washington University in St. Louis,  
 Center of Materials Innovation,  
 Department of Physics, St. Louis, Missouri 63130*

L R Ram-Mohan  
*Departments of Physics, Electrical and Computer Engineering,  
 Worcester Polytechnic Institute, Worcester, MA 01609*

(Dated: September 24, 2018)

For applications to sensor design, the product  $n \times \mu$  of the electron density  $n$  and the mobility  $\mu$  is a key parameter to be optimized for enhanced device sensitivity. We model the carrier mobility in a two dimensional electron gas (2DEG) layer developed in a  $\delta$ -doped heterostructure. The sub-band energy levels, electron wave functions, and the band-edge profile are obtained by numerically solving the Schrödinger and Poisson equations self-consistently. The electron mobility is calculated by including contributions of scattering from ionized impurities, the background neutral impurities, the deformation potential acoustic phonons, and the polar optical phonons. We calculate the dependencies of  $n \times \mu$  on temperature, spacer layer thickness, doping density, and the quantum well thickness. The model is applied to  $\delta$ -doped quantum well heterostructures of AlInSb-InSb. At low temperature, mobilities as high as  $1.3 \times 10^3 \text{ m}^2/\text{V}\cdot\text{s}$  are calculated for large spacer layers (400 Å) and well widths (400 Å). The corresponding room temperature mobility is  $10 \text{ m}^2/\text{V}\cdot\text{s}$ . The dependence of  $n \times \mu$  shows a maximum for a spacer thickness of 300 Å for higher background impurity densities while it continues to increase monotonically for lower background impurity densities; this has implications for sensor design.

PACS: 72.21.-b

PACS numbers:

## I. INTRODUCTION

In a number of magnetic sensor applications [1-2] the basic considerations for improved sensor performance are using ultra-thin films, of thicknesses  $< 100 \text{ nm}$ , and very high ( $> 1 \text{ m}^2/\text{V}\cdot\text{s}$ ) room temperature mobility. However, it is also important to optimize the product of the carrier density,  $n$ , and the mobility,  $\mu$ , in these devices since they have sensitivity that is proportional to the square of the mobility [3-4], and because high electron concentrations  $n$  and electron mobility  $\mu$  tend to reduce the temperature variation of the sensor output [1, 4].

The mobility in the lateral or in-plane direction, in a layered heterostructure, is substantially enhanced through selectively doping specific regions [5]. Consider a quantum well made up of two layers of compound semiconductor alloys, acting as the barrier regions, on either side of a layer with a smaller energy bandgap. On doping the barrier regions with impurities, the bound carriers are released into the quantum well which has accessible energy levels that are lower than the impurity donor energy levels in the barrier region. If the barrier region has impurity atoms only on one side, the released

free carriers are confined to a narrow region close to the barrier-well interface, forming a two-dimensional electron gas (2DEG) [6]. The local separation of the charges leads to substantial bending of the conduction band-edge, as in figure 1. The carriers occupy sub-band energy levels in the quantum well and are held in the layer by the positively charged ionized donors left behind in the barrier. The ionized impurity scattering in lateral transport in the quantum well layer, due to the placing of the impurities in the barrier regions, can be substantially decreased further by set-back doping [7].

In this paper, we are concerned with calculating the dependence of the mobility on the spacer layer thickness  $d_s$ , quantum well thickness  $d_w$ , temperature  $T$  and the doping density  $N_d$  in a delta-doped layer in the barrier. The use of delta-doping with a spacer layer leads to a very large mobility for the carriers. We also work with the AlInSb-InSb system in which the band gap and the electron effective mass in the lateral direction are small, which is an advantage for obtaining enhanced mobility as high as  $4.1 \text{ m}^2/\text{V}\cdot\text{s}$  at room temperature [8],  $20.9 \text{ m}^2/\text{V}\cdot\text{s}$  at  $77 \text{ K}$  [8], and  $28.0 \text{ m}^2/\text{V}\cdot\text{s}$  at  $7 \text{ K}$  [9], in ultra thin-film structures. This attractive property based on the presence of the InSb layer has been used in obtaining extraordinarily high magnetoresistance (EMR) in semiconductor-metal hybrid structures[4]. While a number of papers in the literature treat the AlGaAs-GaAs [10-14]system theoretically, there are only a few that deal

\*Fax: 314-935-5983

; Electronic address: solin@wustl.edu

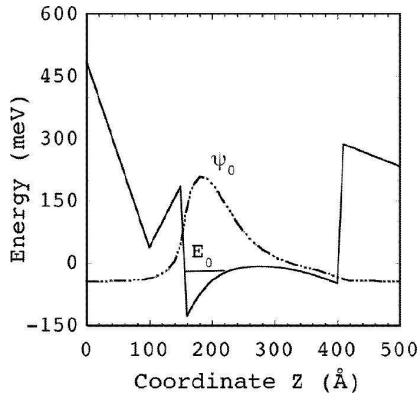


FIG. 1: Figure 1. The conduction band bending, the ground state energy level and its wave function in the  $\delta$ -doped layered heterostructure are shown.

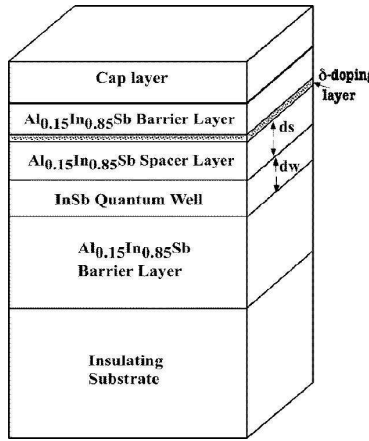


FIG. 2: Figure 2. A schematic diagram of a  $\delta$ -doped  $\text{Al}_{0.85}\text{In}_{0.15}\text{Sb}$ -InSb heterostructure.

with transport properties of the AlInSb-InSb structures [15].

In the following, in Sec. II, we describe the calculation of the energy levels in the heterostructure by solving Schrödinger's equation, and the corresponding wavefunctions, together with the solution of the Poisson equation for the band edge potential given the redistribution of the charges. In Sec. III, we evaluate the carrier mobility by determining the lifetimes for scattering from the impurities and from phonons. Concluding remarks are relegated to Sec. IV.

## II. SOLVING THE SCHRÖDINGER AND POISSON EQUATIONS

We first provide an outline of the method. The Schrödinger and Poisson equations are solved iteratively by first starting with the original band edge profile with no band bending. The wavefunctions obtained for the electron in the original potential are used to determine the charge distribution of the electrons, and this carrier

charge density together with the ionized donor charge density at the delta-doped layer are used as the source terms for Poisson's equation. The change in the band edge profile due to the redistribution of the charges is solved for and a fraction of the change (under-relaxation) in the potential is added to the Schrödinger's equation to initiate the next iteration. At each iteration, the Fermi level is determined through the charge neutrality of the structure as a whole. Convergence is reached when the potential function  $V$  changes by less than 0.1 meV over the last iteration [12].

### 2.1 Solution of the Schrödinger and the Poisson equations

We consider the AlInSb-InSb structure shown in figure 2. The donors in the  $\delta$ -doped layer release electrons into the quantum well layer. These electrons are held close to the quantum well interface by the ionized impurities left behind and form a 2DEG in the triangle-shaped potential created by this redistribution of the charges.

In the effective mass approximation [16-17] we assume that the envelope functions of the electrons are propagating solutions in the in-plane ( $x, y$ )-direction and the  $z$ -dependent envelope function satisfies the one-band equation

$$-\frac{\hbar^2}{2} \frac{d}{dz} \left( \frac{1}{m_z^*} \frac{d}{dz} \psi_n \right) + (E_{CB}(z) + V(z)) \psi_n = \varepsilon_n \psi_n. \quad (2.1)$$

Here,  $m_z^*$  is the effective mass in each layer,  $E_{CB}$  is the original band-edge profile while the potential energy due to the redistribution of the charges is  $V(z)$ . We neglect nonparabolicity [18] of the conduction band energy dispersion. We solve the above equation by the finite element method (FEM) [19-20].

The one dimensional Poisson equation is

$$\frac{d}{dz} \left( \varepsilon \varepsilon_r(z) \frac{dV(z)}{dz} \right) = -e \rho_e = -e^2 [n(z) - N_d(z)], \quad (2.2)$$

where  $\varepsilon_r$  is the relative dielectric constant.  $N_d$  is the ionized donor concentration,  $n(z)$  is the electron density in the Hartree approximation, and  $\rho_e$  is the charge distribution [12, 20]. The electron density distribution is related to the wave function and subband electron occupation by

$$n(z) = \sum_{i=1}^{n_d} n_i^{2D} |\psi_i(z)|^2. \quad (2.3)$$

Here  $n_i^{2D}$  is the electron occupation for each state given by

$$n_i^{2D} = \frac{m^* k_B T}{\pi \hbar^2} \ln \left( 1 + e^{\frac{E_f - E_i}{k_B T}} \right), \quad (T > 0);$$

$$n_i^{2D} = \frac{m^*}{\pi \hbar^2} \Theta(E_f - E_i), \quad (T = 0).$$

$$\quad (2.4)$$

where  $E_f$  is the Fermi energy and  $E_i$  is the subband energy of the bound states in the quantum well, and  $\Theta$  is

the step-function. The self-consistent potential  $V(z)$  depends on  $\rho_e$  which in turn depends on  $E_i$  and  $\psi_i$  obtained from the solution of the Schrödinger equation.

We seek bound state solutions to the Schrödinger equation with  $\psi(0) = 0$  at  $z=0$  at the top of the heterostructure and  $\psi(L) = 0$  at the bottom. At layer interfaces, the wavefunction continuity and the mass-derivative of the wavefunction,  $\psi'/m^*$ , are assumed to be continuous [21]. The boundary conditions for the Poisson equation are:  $V(z=0) = V_c$ , a contact potential, and  $V(z=L) = 0$ , at the bottom of the heterostructure. At layer interfaces, we require that  $V$  and  $\varepsilon_r dV/dz$  be continuous. In order to solve Eqs. (2.1-2.4) self-consistently, we start with the initial choice for the potential function,  $V=0$ , and solve the Schrödinger equation for the bound state energies  $\varepsilon_n$  and wavefunctions  $\psi^{(0)}$ . From this we construct the first approximation to the charge density  $\rho_e$ . Now Poisson's equation is solved to determine the change in the potential energy,  $V(z)$ , with the source terms given by the charge density  $-e[n(z) - N_d(z)]$ . A fraction of this potential energy function is added to the potential energy used in the Schrödinger equation. Letting  $k$  be the iteration index, we set  $V^{k+1}(z) = \alpha \cdot V^k(z) + (1 - \alpha) \cdot V^{k-1}(z)$ , where  $\alpha$  is  $\sim 0.01$ . This is used, in turn, in the Schrödinger equation for the next iteration of the wavefunction  $\psi_n^{k+1}$  using

$$-\frac{\hbar^2}{2} \frac{d}{dz} \left( \frac{1}{m_z^*} \frac{d}{dz} \psi_n^{k+1} \right) + (E_{CB} + V^k) \psi_n^{k+1} = \varepsilon_n^{k+1} \psi_n^{k+1}. \quad (2.5)$$

These wavefunctions are used in defining  $n^{k+1}(z)$  in the source term in Poisson's equation

$$\frac{d}{dz} \left( \varepsilon_0 \varepsilon_r \frac{dV^{k+1}}{dz} \right) = -e \rho_e^{k+1} = -e^2 [n^{k+1}(z) - N_d(z)]. \quad (2.6)$$

The process is repeated until convergence is reached through the criterion that the change in the potential function reaches the tolerance  $\lambda$  such that

$$\frac{|V^{k+1}(z) - V^k(z)|}{|V^k(z)|} \leq \lambda. \quad (2.7)$$

The tolerance was chosen to be  $\lambda \cong 1 \times 10^{-3}$ . The resulting conduction band edge profile is shown in figure 1, together with the ground state wavefunction. The conduction band edge  $E_{CB}$  in each layer is determined by a parameter,  $\gamma$ , representing the conduction band offset in the layer with respect to the band-gap,  $E_g$ , in the material and a reference layer. We include the temperature dependence of the band gap as given by the empirical Varshni equation [22]

$$E_g(T) = E_g(T=0) - \frac{\alpha T^2}{T + \beta}, \quad (2.8)$$

where  $\alpha$  and  $\beta$  are the usual Varshni parameters [23].

For all the ternary alloys, the composition-dependent bandgap is given by a simple linear or quadratic equation as a function of concentration  $x$  by [24-25]

$$E_g(A_{1-x}B_x) = (1 - x) E_g(A) + x E_g(B) - x(1 - x) C. \quad (2.9)$$

Where  $C$  is the bowing parameter for the bandgap, and accounts for the deviation from a linear interpolation between the bandgaps of the two binaries  $A$  and  $B$  [23].

## 2.2 The determination of the Fermi level

As the electrons fall into the quantum well the band-edge potential in the well region moves upwards to make it less energetically unfavorable for the next electron to enter the well region. If band nonparabolicity is ignored, the 2DEG density is given by [11]

$$n_s = \frac{(E_f - E_0) m^*}{\pi \hbar^2}. \quad (2.10)$$

If the barrier doping density is large, the location of the Fermi level is defined by the energy level of the unionized donor and charge neutrality requires that

$$\sum n_s = \sum N_d. \quad (2.11)$$

The Fermi level can be determined by using a root-finding procedure. Equation (2.11) is solved for the Fermi level in every iteration, in order to speed up the convergence.

## III. CALCULATION OF THE MOBILITY

The carrier mobility,  $\mu = e\tau/m^*$ , is governed by scattering mechanisms that control the scattering time,  $\tau$ , associated with each scattering process in a 2DEG [26]. The scattering rates calculated with each scattering mechanism are combined to determine the resultant mobility. The dominant scattering mechanisms for bulk III-V compounds are now well established [27-29]. In our calculations, we have included these mechanisms in the context of 2D scattering.

### 3.1 The scattering from ionized impurities

At low temperature, scattering is dominated by the ionized donors. In a  $\delta$ -doped structure with a spacer layer, the ionized donors and the 2D electrons are spatially separated, thereby minimizing the scattering. We assume that the electron gas is highly degenerate and that the scattering occurs only with electrons near the Fermi level. The transport scattering rate for a purely 2D electron gas, neglecting the electronic wavefunction normal to the plane of the 2D gas, is given by [16]

$$\frac{1}{\tau_{tr}} = N_{imp}^{2D} \frac{m^*}{2\pi\hbar^3 k_F^3} \int_0^{2k_F} \left| \tilde{V}(q) \right|^2 \frac{q^2 dq}{\sqrt{1 - \left( \frac{q}{2k_F} \right)^2}} \quad (3.1)$$

where  $k_F = \sqrt{n_s^{2D} \cdot 2\pi}$  is the Fermi wavevector,  $n_s^{2D}$  is the sheet density of the 2DEG,  $N_{imp}^{2D}$  is the impurity doping areal density and  $\tilde{V}(q) = \int V(r) e^{-i\vec{q} \cdot \vec{r}} d^2 \vec{r}$  is the

Fourier transform of the scattering potential.

Using Thomas-Fermi screening, the scattering rate for remote impurities becomes [16]

$$\frac{1}{\tau_{tr}^{imp}} = n_{imp}^{2D} \frac{m^*}{2\pi\hbar^3 k_F^3} \left( \frac{e^2}{2\varepsilon_0\varepsilon_r} \right)^2 \int_0^{2k_F} \frac{e^{-2q|d|}}{[q + q_{TF}G(q)]^2} \left( \frac{b}{b+q} \right)^6 \frac{q^2 dq}{\sqrt{1 - \left( \frac{q}{2k_F} \right)^2}}, \quad (3.2)$$

with

$$G(q) = \frac{1}{8} \left[ 2 \left( \frac{b}{b+q} \right)^3 + 3 \left( \frac{b}{b+q} \right)^2 + 3 \left( \frac{b}{b+q} \right) \right],$$

and  $b = \left( \frac{33m^*e^2n_{2D}}{8\hbar^2\varepsilon_0\varepsilon_r} \right)^{1/3}$ . The scattering potential takes account of screening with the Thomas-Fermi dielectric function [30]. Here  $q_{TF} = \frac{m^*e^2}{2\pi\hbar^2\varepsilon_r}$  is the screening wavevector in the Thomas-Fermi approximation. The contribution to the mobility from ionized impurity scattering is essentially independent of temperature [31].

### 3.2 The ionized background impurities

The background density of ionized donor impurities is usually very small as compared with ionized impurities with thin spacer layer thickness. But when the thickness of the spacer layer is very large, the effect of remote ionized impurities is reduced and the background impurity scattering dominates. The rate for scattering from the low density background impurities with a concentration of  $N_{bg-imp}^{3D}$  is given by [16]

$$\frac{1}{\tau_{tr}^{bg}} = N_{bg-imp}^{3D} \frac{m^*}{2\pi\hbar^3 k_F^3} \left( \frac{e^2}{2\varepsilon_0\varepsilon_r} \right)^2 \int_0^{2k_F} \frac{1}{(q + q_{TF})^2} \frac{qdq}{\sqrt{1 - \left( \frac{q}{2k_F} \right)^2}}. \quad (3.3)$$

### 3.3 The scattering from phonons

Phonons dominate scattering at high temperature, typically above 60 K [32]. The most important phonon scattering processes in general are: (i) deformation potential acoustic phonon scattering, (ii) polar optical phonon scattering, and (iii) piezoelectric scattering [33-34]. However, Basu and Nag [35] have shown that for InSb, the piezoelectric scattering does not play an important role at intermediate temperatures. We will therefore not consider it here. We consider the electrons to be quasi-two dimensional while the phonons remain quasi-three-dimensional, in which approximation the perturbing potential has a spherical symmetry [16]. For the sake of simplicity, we assume that in the ideal case we have at hand bulk phonons.

The deformation potential acoustic phonon scattering rate is given by [32, 36]

$$\frac{1}{\tau_{tr}^{acoustic}} = \frac{3m^*k_B T \Xi^2}{2\rho v_s^2 \hbar^3 d}. \quad (3.4)$$

where  $\Xi$  is the deformation potential, and  $\rho, v_s$  are the

mass density and the velocity of sound.

The scattering rate by polar optic phonons is given by [32-33]

$$\frac{1}{\tau_{tr}^{polar}} = \frac{k_0 e^2 \pi N_0}{2\hbar\varepsilon_p}, \quad (3.5)$$

with  $N_0 = \left( e^{\frac{\hbar\omega_0}{k_B T}} - 1 \right)^{-1}$ ,  $k_0 = \sqrt{\frac{2m^*\omega_0}{\hbar}}$ , and  $\frac{1}{\varepsilon_p} = \frac{1}{\varepsilon_\infty} - \frac{1}{\varepsilon_r}$ , with  $\varepsilon_\infty$  being the high frequency dielectric constant and  $\varepsilon_r$  being the static dielectric constant. Here  $\hbar\omega_0$  is the optical-phonon energy. Several values (7.2 eV and 30 eV [37-38]) have been quoted in the literature for the deformation potential in InSb. Since the mobility is inversely proportional to  $\Xi^2$ , these different  $\Xi$  values can lead to a large difference in the acoustic phonon scattering contribution to the mobility. We use a value of 7.2 eV for  $\Xi$  in InSb, which was first obtained by Ehrenreich [39] and Dutta [38] who showed that it agrees well with the experimental results.

### 3.4 Other scattering mechanisms

The alloy-disorder scattering by free carriers was neglected in this calculation. Interface (or surface) roughness scattering is another scattering mechanism which has been found to be important in thin quantum wells [40], playing a significant role only at high electron concentrations [41], and thin quantum wells ( $L < 60 \text{ \AA}$ ) [42]. When the first excited subbands become filled with electrons, there will be interface scattering, which would reduce the mobility [43].

### 3.5 The combined mobility

The total mobility is given by computing the mobility for each scattering process and adding the reciprocal mobility for each process according to Mathieson's rule.

$$\frac{1}{\mu_{total}} = \frac{1}{\mu_{imp}} + \frac{1}{\mu_{bg}} + \frac{1}{\mu_{acoustic}} + \frac{1}{\mu_{polar}}. \quad (3.6)$$

At high temperature, the relation may not be valid due to the limited applicability of degenerate statistics [31]. However, for temperatures higher than 60 K the scattering in the 2DEG is dominated by the phonon scattering processes. The approximation has a negligible effect on the combined electron mobility. Therefore we still can use Mathieson's rule to roughly estimate the combined mobility.

The mobility contributions caused by ionized impurity and background impurity scatterings at low temperatures are temperature independent, above the temperature at which the total mobility shows the  $T^{-1}$  dependence.

## IV. RESULTS AND DISCUSSION

We studied the  $\text{Al}_{0.85}\text{In}_{0.15}\text{Sb}$ -InSb system. Some relevant parameters used in the calculation are given in Table 1. The other material parameters employed here have been obtained from Ref. 23. **Table 1.** Parameters used in the calculation are shown.

Parameters of InSb	Value
Effective mass ratio ( $m^*/m_0$ )	0.0135 <sup>a)</sup>
Static dielectric constant ( $\epsilon_0$ )	16.82 <sup>a)</sup>
High-frequency dielectric constant ( $\epsilon_\infty$ )	15.7 <sup>b)</sup>
Lattice density ( $\text{g}/\text{cm}^3$ )	5.79 <sup>b)</sup>
Velocity of longitudinal elastic waves ( $\text{cm}/\text{s}$ )	$3.7 \times 10^5$ <sup>b)</sup>
Acoustic deformation potential (eV)	7.2 <sup>c)</sup>
Optical phonon energy (meV)	25.0 <sup>b)</sup>

<sup>a)</sup> Ref. 23 <sup>b)</sup> Ref. 15 <sup>c)</sup> Ref. 37

### 4.1 Temperature dependence of the electron mobility

The calculated electron mobility, in the range of 1-280 K, is given for the AlInSb-InSb system in figure 3. The components of the mobility contributing to the total mobility are also presented. In figure 3(a),

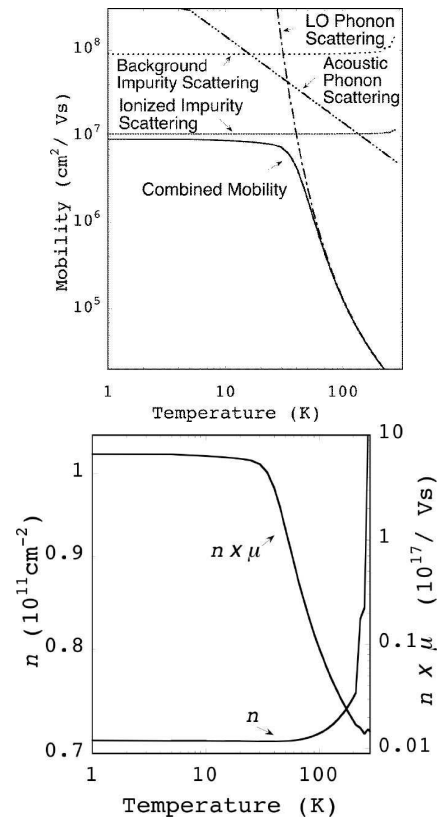


FIG. 3: Figure 3. The temperature dependence of the electron mobility in the  $\text{Al}_{0.85}\text{In}_{0.15}\text{Sb}$ -InSb system is shown. (a) The curves show the calculated mobility with scattering due to the remote ionized impurities with a sheet density of  $1 \times 10^{12} \text{ cm}^2$ . The spacer layer thickness and well thickness are  $400 \text{ \AA}$ . The background impurity density is assumed to be  $5 \times 10^{15} \text{ cm}^{-3}$ . (b) The temperature dependence of the electron subband density and the product of the carrier density and the mobility,  $n \times \mu$ , are shown.

with  $T$  decreasing from 280 K, the carrier mobility increases monotonically and saturates around 30 K. This is in contrast to the bulk semiconductor, where the mobilities tend to peak at intermediate temperature. This is due to the fact that at low temperature, the electron mobility is limited by ionized impurity scattering and phonon-limited scattering is negligible; on the other hand, at high temperature polar-optical-phonon scattering is the dominant scattering mechanism. At intermediate temperature, the deformation-potential acoustic phonon scattering also plays an important role. At high temperature, the mobility shows the expected  $T^{-1}$  dependence. The subband electron occupation is shown in figure 3(b). In our case, only the ground state subband is filled. The electron density in the quantum well remains constant at low temperature. But it increases rapidly about 100 K. We know that for the sensor application, high electron density determines the conductivity and this is as important as the need for high electron mobility. We have therefore plotted the

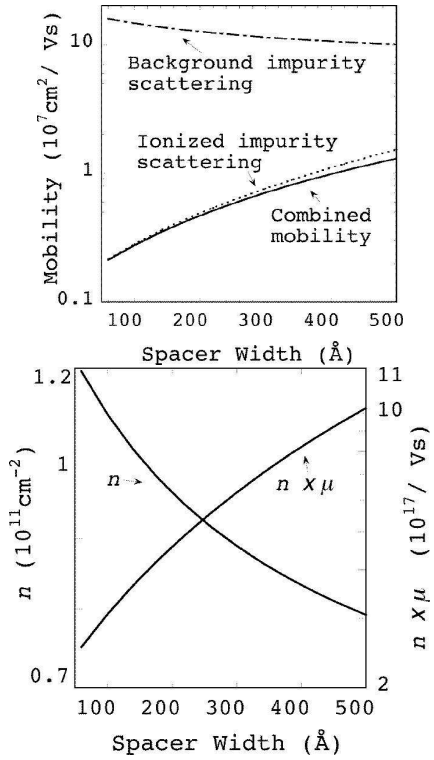


FIG. 4: Figure 4. (a)The dependence of the electron mobility on the thickness of the spacer layer in the  $\text{Al}_{0.85}\text{In}_{0.15}\text{Sb}$ -InSb heterostructure is shown. The calculation is performed at  $T=0$  K for a well width of  $200$  Å. The background impurity density is assumed to be  $5\times 10^{15}\text{cm}^{-3}$ . (b) The dependence of electron subband density and the product of the carrier density and the mobility,  $n\times\mu$ , on the spacer layer thickness are shown.

product of electron density  $n$  and mobility  $\mu$  in figure 3(b). The product of  $n\times\mu$  decreases rapidly at high temperature, and remains constant at low temperature.

#### 4.2 Spacer thickness dependence

The purpose of a  $\delta$ -doped heterostructure is to separate the 2DEG from the parent ionized donors, thereby limiting ionized impurity scattering from the remote doping centers. Figure 4(a) shows that an increase in the spacer thickness leads to an increase in the combined mobility. The ionized impurity mobility increases with increasing spacer thickness, reaching mobilities of  $1\times 10^7\text{ m}^2/\text{Vs}$  at a spacer width of  $400$  Å. The mobility caused by the introduction of background ionized impurities shows the reverse trend. The background impurity mobility decreases with increasing spacer width and becomes dominant. However, an increase of spacer layer thickness leads to a decrease in the electron density  $n$  in the quantum well as shown in figure 4(b). The product  $n\times\mu$  and the carrier density  $n$  are also shown in figure 4(b), with the former increasing with spacer layer thickness.

For a background density of  $5\times 10^{15}\text{ cm}^{-3}$ , the spacer

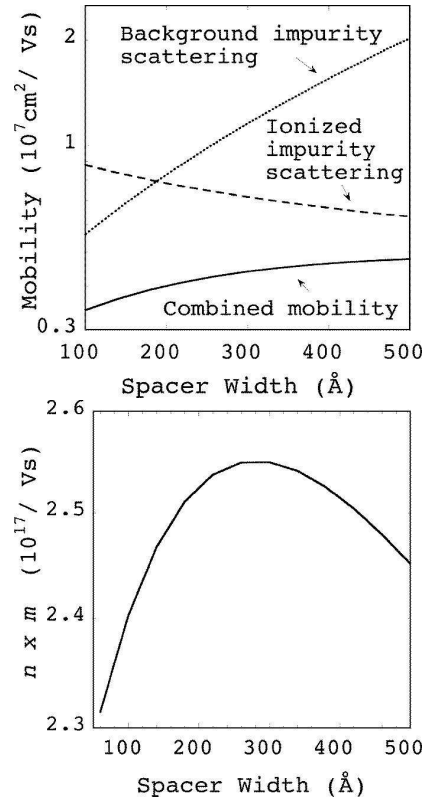


FIG. 5: Figure 5. (a) The dependence of the electron mobility on the spacer layer thickness in the  $\text{Al}_{0.85}\text{In}_{0.15}\text{Sb}$ -InSb heterostructure is shown. The background impurity density is assumed to be  $5\times 10^{16}\text{cm}^{-3}$ . (b) The product of the carrier density and the mobility,  $n\times\mu$ , is shown as a function of the spacer layer thickness.

width dependence of combined mobility is insensitive to the background impurity as can be seen in figure 4(a). However, higher background impurity concentrations will make the background impurity mobility comparable with the ionized impurity mobility which will result in the combined mobility displaying a peak at some spacer thickness, as shown in figure 5. Figure 5(b) also shows that  $n\times\mu$  as a peak value at a spacer width around  $300$  Å at high background impurity density.

#### 4.3 Dependence on the quantum well width

For the well width dependence study we considered the system with a constant spacer layer thickness of  $200$  Å. Figures 6(a) and (b) show that at  $0$  K for a thin quantum well ( $< 200$  Å), electron density  $n$  and  $n\times\mu$  increase rapidly up to  $d_w \sim 200$  Å, while at larger well width, they increase slowly and saturate at a well width  $300$  Å. With the increase in the well width, the background impurity mobility increases faster than the ionized impurity mobility and is a less important factor in the combined mobility. The electron density  $n$  and the product  $n\times\mu$  show the same trend with increasing well width.

Equations (3.4)-(3.6) show that the acoustic-phonon

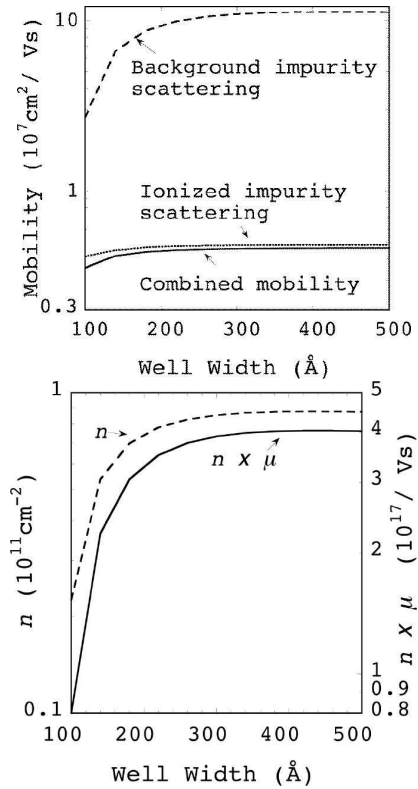


FIG. 6: Figure 6. (a) The dependence of the electron mobility on the well width in the  $\text{Al}_{0.85}\text{In}_{0.15}\text{Sb-InSb}$  heterostructure is shown. The calculation is performed at  $T=0$  K and a spacer layer thickness of  $200$   $\text{\AA}$ . A background impurity density of  $5 \times 10^{15} \text{ cm}^{-3}$  is assumed. (b) The dependence of electron subband density, and of the product of the mobility and electrons,  $n \times \mu$ , on the well layer thickness is shown.

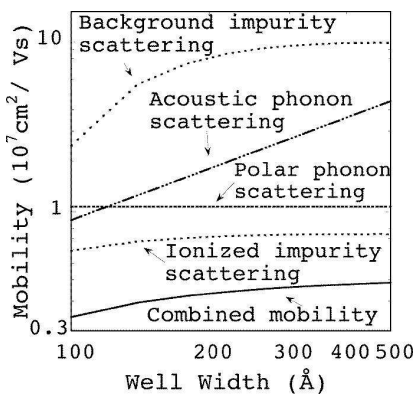


FIG. 7: Figure 7. The dependence of the electron mobility on the well layer thickness in the  $\text{Al}_{0.85}\text{In}_{0.15}\text{Sb-InSb}$  heterostructure is shown on a log-log plot, so that the dependence of polar phonon scattering on well width is shown to be nearly constant. The calculation is performed with  $T=40$  K and a spacer thickness of  $300$   $\text{\AA}$ .

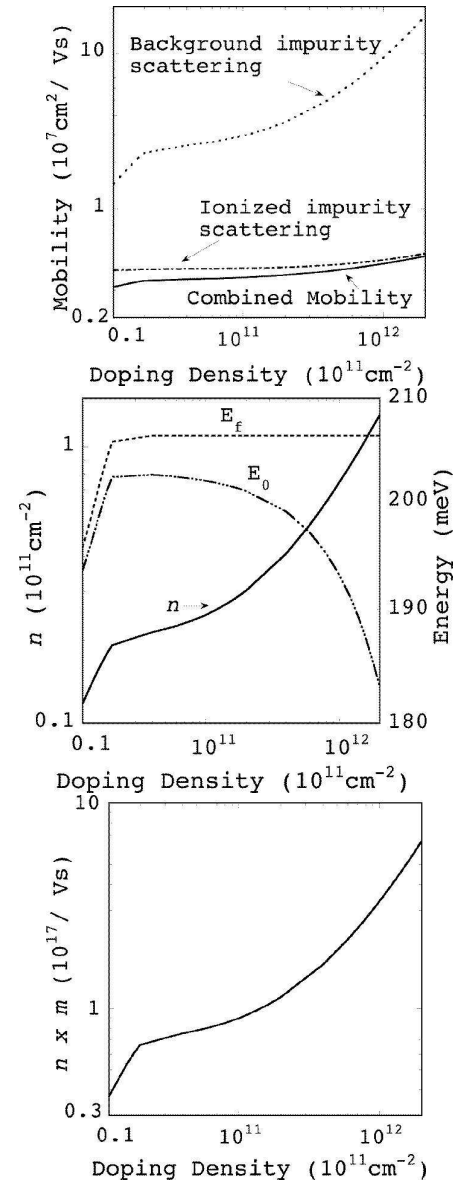


FIG. 8: Figure 8. (a) The dependence of the electron mobility on the doping density in the  $\text{Al}_{0.85}\text{In}_{0.15}\text{Sb-InSb}$  heterostructure is shown. The calculation is performed with  $T=0$  K and spacer and a well thickness of  $200$   $\text{\AA}$ . The background impurity density is assumed to be  $5 \times 10^{15} \text{ cm}^{-3}$ . (b) The variation of the Fermi level, the ground subband energy and electron densities with the ionized doping density are shown. (c) The product of mobility and electron density,  $n \times \mu$ , versus the doping density is shown.

mobility should increase linearly with the well width at intermediate temperature, and that the polar optic phonon scattering remains constant. Figure 7 shows the calculated mobility at  $40$  K. Background impurity and ionized impurity mobility show a similar trend compared to the  $0$  K mobility (Fig. 6a).

#### 4.4 Doping density dependence

Figure 8 shows that at 0 K as the remote impurity density increases, the background impurity mobility increases faster than the ionized impurity mobility. This follows logically, because with more electrons in the quantum well, the effect of background impurities is not the limiting factor in the combined mobility, therefore it shows a trend similar to that of the electron subband density in figure 8(b). At low doping density, all the electrons can enter the well without pushing the Fermi energy up to the conduction band edge. With increased doping density, more electrons can enter the well, and the Fermi energy reaches the conduction band-edge and is unable to move up further. The ground subband energy will then be lower to let more electrons into the well as shown in figure 8(b).

## V. CONCLUSION

In conclusion, we have presented theoretical calculations for the electron subband energy, subband electron density, and carrier mobility in  $\delta$ -doped single quantum well heterostructures. Here, the Hartree approximation for the confinement potential was used. The important scattering mechanisms, such as, ionized impurity scattering, background impurity scattering, deformation potential acoustic phonon scattering, and polar phonon scat-

tering were considered. We have presented the behavior of the product of electron mobility and density in the temperature range of 0 - 280 K as a function of the spacer layer thickness, well width, and doping density.

At low temperature, the dominant scattering mechanism is ionized impurity scattering. It is also found to be independent of temperature in this regime. In the AlInSb-InSb system, the mobility due to ionized impurity scattering increases with decreasing temperature, reaching a limiting value of about  $1 \times 10^7 \text{ cm}^2/\text{V}\cdot\text{s}$  for a thicker well and larger spacer ( $>300 \text{ \AA}$ ) at low temperature (0 K). At a temperature around 40 K, optical phonons begin to limit the mobility which varies as  $T^{-1}$  at high temperature. The dependence of  $n \times \mu$  shows a maximum for a spacer thickness of 300  $\text{\AA}$  for higher background impurity densities while it continues to increase monotonically for lower background impurity densities.

## Acknowledgments

This work was supported by the NSF (Grant No. ECS-0329347) and the Center for Materials Innovation at Washington University. LRR thanks Washington University in St. Louis for the Harrison Fellowship which supported his collaborative visit during part of which this work was carried out.

---

[1] Zhou T, Solin S A and Hines D T 2001 *J. Magn. Magn. Mater.* **226** 1976-7.

[2] Solin S A, Thio T, Hines D R and Heremans J J 2000 *Science* **289** 1530-2.

[3] Solin S A, Hines D R, Rowe A C H, Tsai J S, Pashkin Yu A, Chung S J, Goel N and Santos M B 2002 *Appl. Phys. Lett.* **80** 4012-4.

[4] Solin S A, Hines D R, Tsai J S, Pashkin Yu A, Chung S J, Goel N and Santos M B 2002 *IEEE Trans. Magn.* **38** 89-94.

[5] Dingle R, Störmer H L, Gossard A C and Wiegmann W 1978 *Appl. Phys. Lett.* **33** 665-7.

[6] Ando T, Fowler A B and Stern F 1982 *Rev. Mod. Phys.* **54** 437-672.

[7] Hiyamizu S, Saito J, Nanbu K and Ishikawa T 1983 *Jpn. J. Appl. Phys.* **22** L609-11.

[8] K J Goldammer, Liu W K, Khodaparast G A, Lindstrom S C, Johnson M B, Doezeema R E and Santos M B 1998 *J. Vac. Sci. Technol. B* **16** 1367-71.

[9] Chung S J, Goldammer K J, Lindstrom S L, Johnson M B and Santos M B 1999 *J. Vac. Sci. Technol. B* **17** 1151-4.

[10] Trellakis A, Galick A T, Pacelli A and Ravaioli U 1997 *J. Appl. Phys.* **81** 7880-4.

[11] Stern F 1983 *Appl. Phys. Lett.* **43** 974-6.

[12] Ram-Mohan L R, Yoo K H and Moussa J 2004 *J. Appl. Phys.* **95** 3081-92.

[13] Inoue K, Sakaki H, Yoshino J and Hotta T 1985 *J. Appl. Phys.* **58** 4277-81.

[14] Tan I, Snider G L, Chang L D and Hu E L 1990 *J. Appl. Phys.* **68** 4071-6.

[15] See, for example, Ozbas O and Akarsu M 2002 *Turk J. Phys.* **26** 283-7.

[16] Davies J 1998 *The Physics of Low-Dimensional Semiconductors* (Cambridge University Press, New York, NY, USA) p290-366.

[17] Bastard G 1988 *Wave mechanics applied to semiconductor heterostructures* (Editions de Physique, Les Ulis, France; Halsted Press, New York).

[18] Yoo K H, Ram-Mohan L R and Nelson D F 1989 *Physical Review B* **39** 12808-13.

[19] Ram-Mohan L R, Saigal S, Dossa D and Shertzer J 1990 *Computers in Physics* **4** 50-9.

[20] Ram-Mohan L R *Finite Element and Boundary Element Applications to Quantum Mechanics* 2002 (Oxford University Press, NY, USA).

[21] BenDaniel D J and Duke C B 1966 *Phys. Rev.* **152** 683-92.

[22] Varshni Y P 1967 *Physica (Utrecht)* **34** 149.

[23] Vurgaftman I, Meyer J R and Ram-Mohan L R 2001 *J. Appl. Phys.* **89** 5815-75.

[24] Van Vechten J A and Bergstresser T K 1970 *Phys. Rev. B* **1** 3351-8.

[25] Wright A F and Nelson J S 1995 *Appl. Phys. Lett.* **66** 3465-7.

[26] Störmer H L 1983 *Surf. Sci.* **132** 519-26.

[27] Conwell E and Weisskopf V F 1950 *Phys. Rev.* **77** 388-9.

- [28] Brooks H 1951 *Phys. Rev.* **83** 879.
- [29] Stillman G E and Wolfe C M 1976 *Thin Solid Films* **31** 69-88.
- [30] Ioriatti L 1990 *Phys. Rev. B* **41** 8340-4.
- [31] Walukiewicz W, Ruda H E, Lagowski J and Gatos H C 1984 *Phys. Rev. B* **30** 4571-82.
- [32] Arora V K and Naeem A 1985 *Phys. Rev. B* **31** 3887-92.
- [33] Price P J 1981 *Ann. Phys.* **133** 217-39.
- [34] Arora V K 1982 *Phys. Rev. B* **26** 2247-9.
- [35] Basu P K and Nag B R 1981 *J. Phys. C* **14** 1519-22.
- [36] Ridley B K 1982 *J. Phys. C* **15** 5899-917.
- [37] Nag B R and Dutta G M 1975 *Phys. Stat. Sol. (b)* **71** 401.
- [38] Dutta G M, Chattopadhyay D and Nag B R 1974 *J. Phys. C* **7** 1854-6.
- [39] Ehrenreich H 1957 *J. Phys. Chem. Solids* **2** 131-49.
- [40] Kulbachinskii V A, Kytin V G, Babushkina T S and Malkina I G 1996 .
- [41] Ando T 1982 *J. Phys. Soc. Jpn.* **51** 3900-7.
- [42] Sakaki H, Noda T, Hirakawa H, Tanaka M and Matsusue T 1987 *Appl. Phys. Lett..*